aerospace

MDPI

Article

Real-Fluid Effects on Flame Structure and Stability of Transcritical Liquid-Oxygen/Methane Counterflow Multi-Branch Flames

Ying Bai [1,2], Bo He [2,*], Shengfeng Luo [3], Pengyu Liu [1,2], Wenfeng Hu [1,2] and Weidong Huang [2]

[1] Graduate School, Space Engineering University, Beijing 101416, China
[2] Department of Aerospace Science and Technology, Space Engineering University, Beijing 101416, China
[3] Sino-German College of Intelligent Manufacturing, Shenzhen Technology University, Shenzhen 518118, China
* Correspondence: comhebo@sina.com

Abstract

Laminar counterflow multi-branch flames provide a canonical configuration for investigating interactions between oxidizer-rich and fuel-rich streams in liquid-oxygen/methane combustion systems. This study numerically investigates their flame structure and stability under transcritical conditions, with stability characterized by the extinction strain rate. Ideal-fluid (IF), partial real-fluid (PRF), and real-fluid (RF) models are compared to distinguish the effects of real-fluid thermodynamics and high-pressure transport corrections. The multi-branch flame comprises two premixed branches coupled with a central diffusion branch. Heat release from the premixed branches creates high-temperature plateaus that preheat the stagnation-region mixture and sustain the diffusion branch. Although the three models predict similar flame topologies, the IF model gives an extinction strain rate of $3.306 \times 10^6\ s^{-1}$, whereas both PRF and RF predict $3.256 \times 10^6\ s^{-1}$. Thus, the ideal-fluid treatment slightly overpredicts the extinction limit under the present reference condition, while high-pressure transport corrections influence the ignition location, peak temperature, and thermal diffusivity. Increasing pressure from 10 MPa to 40 MPa raises the extinction strain rate from $9.336 \times 10^5\ s^{-1}$ to $4.867 \times 10^6\ s^{-1}$ by strengthening heat release and reducing thermal diffusion from the high-temperature region. Oxidizer preheating markedly enhances flame stability, whereas fuel preheating has a weak effect. These findings establish the connection between real-fluid thermodynamics, branch interaction, and extinction stability, providing a physical basis for model selection, operating-condition optimization, and stability-margin assessment in transcritical liquid-oxygen/methane combustion systems.

Keywords: liquid-oxygen/methane; transcritical combustion; laminar counterflow flame; multi-branch flame; real-fluid thermodynamics; extinction strain rate

Check for updates

Academic Editor: Angel Velazquez

Received: 14 June 2026
Revised: 24 July 2026
Accepted: 27 July 2026
Published: 30 July 2026

Copyright: © 2026 by the authors. Licensee MDPI, Basel, Switzerland. This article is an open access article distributed under the terms and conditions of the Creative Commons Attribution (CC BY) license.

1. Introduction

Liquid-oxygen/methane propulsion is increasingly relevant to reusable launch systems because it combines high performance with favorable propellant handling and reduced carbon deposition [1]. In a full-flow staged-combustion (FFSC) cycle [2,3], both propellants pass through preburners; the main chamber therefore receives an oxidizer-rich stream and a fuel-rich stream rather than two cold, unmixed reactants. A multi-branch flame consists of an oxidizer-rich premixed flame branch, a fuel-rich premixed flame branch, and a diffusion flame branch [4]. Physically, the multi-branch flame provides a complete description of the full combustion process from the preburner to the main combustor

in the FFSC engine. The oxidizer-rich and fuel-rich premixed branches correspond to the premixed combustion process in the preburners, while the diffusion flame branch corresponds to the combustion process in the main combustor, where the two streams mix and undergo final combustion. Therefore, investigating the flame characteristics of multi-branch flames can provide fundamental insights into the combustion flow field within FFSC engine combustors. In particular, analyzing the effects of pressure and inlet temperature on multi-branch flames directly corresponds to the regulation and control of the oxidizer-rich and fuel-rich preburner inlet parameters in actual FFSC engine operation.

Such interactions occur at high pressure and cryogenic inlet temperature, where thermophysical properties vary strongly with temperature, pressure, and composition. Density, constant-pressure specific heat, viscosity, thermal conductivity, and mass diffusivity may change nonlinearly as the fluid crosses the transcritical region, thereby altering ignition location, heat-release localization, flame thickness, and extinction behavior. Song et al. [5] demonstrated the value of resolving flame structure and stabilization mechanisms in a high-pressure non-premixed hydrothermal flame. Complementary studies have used counterflow flames or flamelet concepts to examine kinetic diagnostics, intermediate-flamelet instability, extinction response, and pressure-dependent temperature distributions in other fuel systems [6–10]. These studies establish the usefulness of canonical flames for separating chemistry, transport, and thermodynamic effects, but their conclusions cannot be transferred directly to cryogenic liquid-oxygen/methane multi-branch flames.

Counterflow diffusion flames have provided the principal foundation for investigating real-fluid effects at elevated pressure. Ribert et al. [11] formulated counterflow diffusion flames for general fluids and showed that real-fluid effects are most pronounced in the transcritical region, whereas the high-temperature reaction zone can approach ideal-gas behavior. Juanos et al. [12] demonstrated that real-fluid thermodynamics can substantially modify density, transport response, and flame structure in high-pressure laminar counterflows. For oxygen/methane flames, Wang et al. [13] reported that the pressure dependence of the extinction strain rate changes between subcritical and supercritical regimes and emphasized the importance of the oxygen injection temperature for evaluating transcritical thermophysical properties. Juanós et al. [14] further showed that high-pressure methane/oxygen extinction depends on mixture composition and dilution state. Collectively, these studies establish the importance of real-fluid modeling, but they primarily concern diffusion-controlled flame structures without coupled premixed branches.

Partially premixed flames introduce additional coupling between premixed reaction and diffusive mixing. Stagni et al. [15] showed that low-temperature chemistry modifies the ignition region of partially premixed n-heptane/air counterflow flames, while increasing strain can suppress this pathway by shortening the residence time. Under transcritical conditions, Lv et al. [16] found that the diffusion model, strain rate, and fuel-rich equivalence ratio reshape the premixed reaction zone. Gao et al. [17] further demonstrated that real-fluid thermodynamic corrections affect both diffusion and premixed flames through changes in heat capacity and related properties. These findings indicate that premixing, aerodynamic strain, and real-fluid thermodynamics are coupled rather than independent influences in high-pressure reacting flows.

The conceptual basis for multi-branch flames originates from triple- and tribrachial-flame theory, in which two premixed branches are coupled to a trailing diffusion branch. Hartley et al. [18] analyzed triple-flame propagation in a nonuniform mixture and related the propagation behavior to local mixture stratification. Kioni et al. [19] described the coupled propagation of leading premixed branches and a trailing diffusion flame in laminar mixing layers. Ruetsch et al. [20] subsequently showed that heat release and thermal expansion modify flame curvature, propagation speed, and branch geometry. Although

these configurations differ from the opposed-flow arrangement considered here, they establish a central principle: a multi-branch flame is a coupled structure rather than a simple superposition of independent premixed and diffusion flames.

Later studies extended this framework to more realistic fuels and operating conditions. Owston et al. [21] showed that mixture stratification, ambient temperature, pressure, and water-vapor concentration modify hydrogen triple-flame behavior. Bisetti et al. [22] demonstrated that n-heptane tribrachial-flame stabilization depends on the interaction between chemical kinetics and the local mixing-layer structure. Chen et al. [23] found that pressure changes the propagation characteristics of methane-air edge flames in two-dimensional mixing layers. These results clarify how pressure, composition, and transport influence branch interaction, but they were not developed for cryogenic liquid oxygen and methane under transcritical pressure.

The counterflow configuration has recently been applied directly to multi-branch flames. López-Cámara et al. [4] showed that pressure and strain rate determine whether multiple branches coexist, merge, or extinguish in multi-branch counterflow flames. Nevertheless, three issues remain insufficiently resolved for transcritical liquid-oxygen/methane combustion. First, the relative contributions of real-fluid thermodynamics and high-pressure transport corrections to flame stability have not been clearly separated. Second, the mechanism by which the two premixed branches support the central diffusion branch under increasing strain requires further clarification. Third, oxidizer and fuel inlet temperatures may affect the two premixed branches asymmetrically, but this response has not been systematically quantified.

In summary, previous studies [11–14] have primarily focused on counterflow diffusion flames with a single diffusion flame structure under transcritical conditions. Research on partially premixed flames [15–17] under these conditions is limited to configurations with only one premixed branch and one diffusion branch. Multi-branch flames remain largely unexplored, particularly in the context of FFSC engines. Furthermore, existing studies [18–23] on multi-branch flames are confined to subcritical conditions, leaving a significant gap in the understanding of their structure and extinction behavior under transcritical conditions.

The present study addresses these questions using a one-dimensional laminar counterflow model of multi-branch liquid-oxygen/methane flames under transcritical conditions. Here, flame stability refers specifically to resistance against strain-induced extinction and is quantified by the extinction strain rate. Ideal-fluid (IF), partial real-fluid (PRF), and real-fluid (RF) models are compared to distinguish the contributions of the equation of state and thermodynamic departure functions from those of high-pressure transport corrections. The study then examines how operating pressure and the oxidizer and fuel inlet temperatures regulate flame structure, heat release, and extinction stability. Particular attention is given to the hypothesis that heat release from the premixed branches preheats the stagnation-region mixture and thereby stabilizes the central diffusion branch. The results provide a physical basis for thermophysical-model selection and stability-margin assessment in high-pressure liquid-oxygen/methane combustion systems.

The remainder of this paper is organized as follows. Section 2 presents the physical model, governing equations, thermodynamic and transport-property treatments, chemical mechanism, and numerical conditions. Section 3 presents the validation of the models and numerical methods, including a grid convergence study, model (thermophysical property and chemical reaction mechanism) validation and algorithm validation. Section 4 first identifies the multi-branch stabilization mechanism, then evaluates sensitivity to the thermophysical-property model, and finally analyzes the effects of pressure and inlet temperature. Section 5 summarizes the principal conclusions.

2. Theoretical Formulation

2.1. Physical Model

Figure 1 shows the idealized laminar counterflow configuration considered in this study. Two opposed premixed streams, one oxidizer-rich and one fuel-rich, are injected into a one-dimensional domain and form a multi-branch flame composed of an oxidizer-rich premixed branch, a fuel-rich premixed branch, and a central diffusion branch. This configuration is not intended to reproduce the full three-dimensional FFSC combustor directly; rather, it extracts the local opposed-flow interaction between oxidizer-rich and fuel-rich streams so that the effects of real-fluid thermodynamics and operating parameters can be isolated.

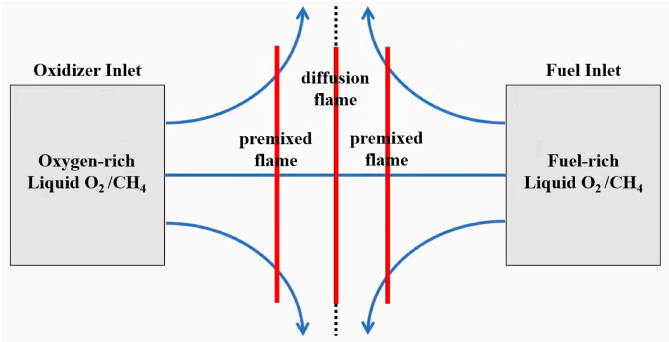


Figure 1. Schematic diagram of the laminar counterflow multi-branch flame configuration. The blue arrow lines represent the propellant propagation process; the dot line represents the flame center location.

In one-dimensional laminar counterflow flames, the global strain rate (a) is defined as [24]:

$$a = \frac{2|u_o|}{L}\left(1 + \frac{|u_f|}{|u_o|}\frac{\sqrt{\rho_f}}{\sqrt{\rho_o}}\right) \tag{1}$$

where the subscripts f and o represent the fuel and oxidizer streams, respectively; u denotes the axial velocity; ρ denotes the density; and L denotes the distance between the two inlets, which is initially set to 3.6 mm in this study. To keep the flame stagnation plane located at the center of the computational domain, the momentum flux is set to be conserved at both inlets, i.e., $\rho_o u_o^2 = \rho_f u_f^2$. Consequently, the inlet velocities for the oxidizer and fuel can be obtained as follows:

$$u_o = \frac{aL}{4} \tag{2}$$

$$u_f = u_o\sqrt{\frac{\rho_o}{\rho_f}} \tag{3}$$

The inlet streams are specified as fresh fuel-rich and oxidizer-rich CH_4/O_2 mixtures and therefore do not reproduce the detailed composition of actual FFSC preburner products, which generally contain H_2O, CO_2, CO, and H_2. This deliberate idealization is adopted to isolate the coupled effects of real-fluid thermodynamics, pressure, and inlet temperature on the three-branch flame structure under controlled conditions. Accordingly, the present configuration should be interpreted as a canonical representation of the relevant local combustion processes rather than a composition-resolved model of an FFSC main combustor.

2.2. Governing Equations

By reducing the axisymmetric counterflow flame to a one-dimensional steady problem, the governing equations for mass, radial momentum, energy, and species conservation can be written as follows [25]:

$$\frac{\partial \rho u}{\partial z} + 2\rho V = 0 \tag{4}$$

$$\rho \mathrm{u}\frac{\partial V}{\partial z} + \rho V^2 = -\Lambda + \frac{\partial}{\partial z}\left(\mu \frac{\partial V}{\partial z}\right) \tag{5}$$

$$\rho c_p u \frac{\partial T}{\partial z} = \frac{\partial}{\partial z}\left(\lambda \frac{\partial T}{\partial z}\right) - \sum_k j_k \frac{\partial h_k}{\partial z} - \sum_k h_k W_k \dot{\omega}_k \tag{6}$$

$$\rho u \frac{\partial Y_k}{\partial z} = -\frac{\partial j_k}{\partial z} + W_k \dot{\omega}_k \tag{7}$$

where ρ is the density, u is the axial velocity, $V = v/r$ is the scaled radial velocity, v is the radial velocity, Λ is the pressure eigenvalue, μ is the dynamic viscosity, c_p is the constant-pressure specific heat, T is the temperature, λ is the thermal conductivity, j_k is the diffusive mass flux of species k, h_k is the enthalpy of species k, and $\dot{\omega}_k$ is the molar production rate of species k. The diffusion terms are evaluated with a multicomponent transport model [26]. The Soret effect is included in this study. All flame structures, extinction limits, and parametric results reported in this study are obtained using this transport treatment.

2.3. Equation of State and Thermodynamic Properties

For ideal fluids, the ideal gas (IG) equation of state is employed to calculate the fluid density, thereby closing the governing equations. It is expressed as:

$$p = \frac{\rho R T}{M} \tag{8}$$

where p is the pressure, R is the universal gas constant, and M is the molar mass of the mixture. Under the ideal-gas assumption, the standard-state thermodynamic properties, including the constant-pressure specific heat c_p^0, enthalpy h^0, and entropy s^0, are calculated using the NASA-7 polynomial parameterization method [27]:

$$c_p^0 = \left(a_0 + a_1 T + a_2 T^2 + a_3 T^3 + a_4 T^4\right) R \tag{9}$$

$$h^0 = \left(a_0 T + \frac{a_1}{2} T^2 + \frac{a_2}{3} T^3 + \frac{a_3}{4} T^4 + \frac{a_4}{5} T^5 + a_5\right) R \tag{10}$$

$$\mathrm{s}^0 = \left(a_0 \ln T + a_1 T + \frac{a_2}{2} T^2 + \frac{a_3}{3} T^3 + \frac{a_4}{4} T^4 + a_6\right) R \tag{11}$$

Here, $a_0 \sim a_6$ are the NASA polynomial coefficients [27,28].

For real fluids, the Peng–Robinson equation of state [29] is employed to account for real fluid effects, which is expressed as:

$$p = \frac{RT}{v - \mathrm{b}} - \frac{a}{v^2 - 2bv - b^2} \tag{12}$$

where v is the specific volume. The parameter a, which is related to the critical temperature T_c, critical pressure P_c, and acentric factor ω of the species, accounts for intermolecular attractive forces. The parameter b represents the molecular co-volume and accounts for the effect of finite molecular volume on fluid behavior. Their expressions are given by:

$$a(T) = a(T_c) \cdot \alpha(T_r, \omega) \tag{13}$$

$$b(T) = b(T_c) \tag{14}$$

The corresponding pure-species parameters and temperature-dependent correction factor are defined as:

$$a(T_c) = 0.45724\frac{R^2 {T_c}^2}{P_c} \tag{15}$$

$$b(T_c) = 0.07780\frac{RT_c}{P_c} \tag{16}$$

$$\alpha^{\frac{1}{2}} = 1 + \kappa\left(1 - T_r^{\frac{1}{2}}\right) \tag{17}$$

$$\kappa = 0.37464 + 1.54226\omega - 0.26992\omega^2 \tag{18}$$

$$T_r = \frac{T}{T_c} \tag{19}$$

The mixture-related parameters are calculated according to the mixing rules [26] which are expressed as:

$$a = \sum_i \sum_j X_i X_j a_{ij} \tag{20}$$

$$b = \sum_i X_i b_i \tag{21}$$

$$a_{ij} = \left(1 - \delta_{ij}\right) a_i^{\frac{1}{2}} a_j^{\frac{1}{2}} \tag{22}$$

where X_i represents the mole fraction of species i, and δ_{ij} is the binary interaction coefficient between species i and j, which is calculated from the correlation in Chueh et al. [30]. For real fluids, the thermodynamic properties are corrected using departure functions [26]:

$$c_p = c_p^0 - T\frac{\left(\frac{\partial p}{\partial T}\right)_\nu^2}{\left(\frac{\partial p}{\partial \nu}\right)_T} - R - T\frac{\partial^2 a}{\partial T^2}\frac{1}{2\sqrt{2}b}\ln\left[\frac{\nu + \left(1 - \sqrt{2}\right)b}{\nu + \left(1 + \sqrt{2}\right)\mathrm{b}}\right] \tag{23}$$

$$h = h^0 + p\nu - RT + \left(a - T\frac{\partial a}{\partial T}\right)\frac{1}{2\sqrt{2}b}\ln\left[\frac{\nu + \left(1 - \sqrt{2}\right)b}{\nu + \left(1 + \sqrt{2}\right)\mathrm{b}}\right] \tag{24}$$

$$\mathrm{s} = \mathrm{s}^0 + R\ln\left[\frac{(\nu - b)p^0}{RT}\right] - \frac{\partial a}{\partial T}\frac{1}{2\sqrt{2}b}\ln\left[\frac{\nu + \left(1 - \sqrt{2}\right)b}{\nu + \left(1 + \sqrt{2}\right)\mathrm{b}}\right] \tag{25}$$

where c_p^0, h^0, and s^0 are the standard-state thermodynamic properties of the ideal fluid mentioned above, and p^0 is the reference pressure, taken as 1 atm.

Furthermore, the integrated heat release rate in this study is defined as the heat flux per unit area, denoted as $\dot{q}_s$:

$$\dot{q}_s = \int_0^L \left(\sum_{k=1}^{N_s} \overline{h}_k W_k \dot{\omega}_k\right) dx \tag{26}$$

where $\overline{h}_k$ is the enthalpy of the k-th species,W_k is the molar mass of the k-th species, and $\dot{\omega}_k$ is the production rate of the k-th species.

2.4. Transport Properties

Viscosity (μ) and thermal conductivity (λ) are typically calculated using the Chung method [31]. For ideal fluids, where the compressibility of the substance under high-

pressure conditions is neglected, the substance remains a dilute fluid. Its calculation formula is given as:

$$\mu^0 = 40.785 \frac{F_c \left(\mathrm{M}T\right)^{\frac{1}{2}}}{v_c^{\frac{2}{3}} \Omega^*} \tag{27}$$

$$\lambda^0 = 3.75 \frac{\mu^0 \mathrm{R} \Psi}{M} \tag{28}$$

where F_c represents an empirical formula dependent on the acentric factor ω and molecular polarity; ν_c denotes the critical volume; Ω^* stands for an empirical formula based on intermolecular potential energy [31]; and Ψ is an empirical correction term.

For real fluids, the substance is considered a dense, compressible fluid under high-pressure environments, necessitating high-pressure corrections to viscosity and thermal conductivity [31]:

$$\mu = \mu^0 \left(\frac{1}{G_2} + A_6 \mathrm{Y} \right) + \mu_p \tag{29}$$

Here, $G_2 = \{A_1[1 - \exp(-A_4 Y)]/Y + A_2 G_1 \exp(A_5 Y) + A_3 G_1\}/(A_1 A_4 + A_2 + A_3)$; $\mu_p = \left[36.344 \times 10^{-6} (M T_c)^{0.5} / v_c^{\frac{2}{3}}\right] A_7 Y^2 G_2 \left(A_8 + A_9/T^* + A_{10} T^{*2}\right)$; $\mathrm{Y} = \rho \nu_c / 6$; $G_1 = (1.0 - 0.5Y)/(1 - Y)^3$; the constants A_1–A_{10} are linear functions of the acentric factor 31; T_c denotes the critical temperature; and T^* denotes the dimensionless temperature.

$$\lambda = \lambda^0 \left(\frac{1}{H_2} + B_6 \mathrm{Y} \right) + \lambda_p \tag{30}$$

Here, $H_2 = \{B_1[1 - \exp(-B_4 Y)]/Y + B_2 G_1 \exp(B_5 Y) + B_3 G_1\}/(B_1 B_4 + B_2 + B_3)$; $\lambda_p = \left[3.039 \times 10^{-4} (T_c/M)^{0.5} / v_c^{\frac{2}{3}}\right] B_7 Y^2 H_2 T_r^{0.5}$; the constants B_1–B_7 are linear functions of the acentric factor, the reduced dipole moment, and the association factor [31]; and $T_r = T/T_c$. The mass diffusion coefficient is determined by the Takahashi method [32].

To assess the relative importance of thermodynamic and transport corrections, three thermophysical-property models are considered: (1) the ideal-fluid (IF) model, in which both thermodynamic and transport properties are evaluated with ideal-fluid assumptions; (2) the partial real-fluid (PRF) model, in which real-fluid thermodynamics are used while transport properties are evaluated with ideal-fluid expressions; and (3) the real-fluid (RF) model, in which both thermodynamic and transport properties include real-fluid corrections.

2.5. Chemical Reaction Mechanism

A reduced methane-oxygen chemical reaction mechanism proposed by Laurent [33], containing 17 species and 62 elementary reactions, is adopted in this study. In this paper, this mechanism is referred to as the reduced mechanism. In addition, the GRI-Mech 3.0 [34] detailed mechanism is adopted in this study as a benchmark to validate the reduced mechanism. A comparison is conducted in Section 3.2 using laminar counterflow multi-branched flames. Throughout this paper, this mechanism is referred to as the detailed mechanism.

2.6. Initial and Boundary Conditions

The standard case is defined as $p = 30$ MPa, $a = 500\ \mathrm{s}^{-1}$, $\mathrm{T_f} = 110$ K, $\mathrm{T_o} = 90$ K, $\varphi_f = 2.0$, and $\varphi_o = 0.5$. These conditions are used as an idealized high-pressure liquid oxygen/methane counterflow case for isolating the basic flame response. An initial temperature and species field based on an error-function profile is imposed to improve numerical convergence.

Dirichlet boundary conditions are applied at the fuel and oxidizer inlets to specify the temperature, mass flow rate, and species mole fractions. This choice follows the standard treatment for opposed-flow diffusion flames [25], as it reflects the physically known state at the nozzle exit plane and provides numerical stability for reactive flow calculations. Dirichlet boundary conditions are given as follows:

$$\mathrm{x} = 0\ \mathrm{mm}:\ \mathrm{T} = \mathrm{T_o};\ \dot{m} = \dot{\mathrm{m}}_\mathrm{o};\mathrm{X_i} = \mathrm{X_{i,o}} \tag{31}$$

$$\mathrm{x} = 3.6\ \mathrm{mm}:\ \mathrm{T} = \mathrm{T_f};\ \dot{m} = \dot{\mathrm{m}}_\mathrm{f};\ X_i = X_{i,f} \tag{32}$$

2.7. Numerical Algorithm

All simulations are performed with Cantera 3.2.0 [35], which provides laminar-flame solvers together with real-fluid thermodynamics and high-pressure transport-property corrections. This section describes the grid processing method and the extinction limit calculation approach adopted in the present study.

2.7.1. Grid Processing Method

When real-fluid effects are considered, a uniform grid with a large number of grid points is required to accurately capture the steep gradients of the laminar flamelet, which significantly increases the computational cost. Therefore, to reduce the computational expense, a non-uniform grid is employed in the present study. Given that the flame characteristics exhibit sharp gradient variations near the flamelet, a higher density of grid points is needed in this region. A Gaussian function is used to control the distribution of grid points, thereby achieving grid clustering in the high-gradient region while conserving computational resources. The Gaussian function is expressed as follows:

$$f(x) = \frac{1}{\sigma\sqrt{2\pi}} exp\left(-\frac{(x-\mu)^2}{2\sigma^2}\right) \tag{33}$$

where μ denotes the mean, and σ denotes the standard deviation. In the Gaussian non-uniform grid, μ represents the flame center location (i.e., the position of the peak flame temperature), and σ controls the extent of the grid clustering region. Figure 2 illustrates the single Gaussian non-uniform grid distribution with 150 grids. The red dashed line represents the flame center position (1.067 mm), which serves as the center of the Gaussian clustering. The blue vertical lines indicate the location of each grid point, with the mesh becoming denser closer to the flame center. The red shaded region denotes the refined area, with a range of $\pm 2\sigma = \pm 500$ µm. The gray vertical lines at the bottom represent a uniform grid with a grid spacing of 13.33 µm. In the Gaussian non-uniform grid, the minimum grid spacing at the flame center can reach 5.70 µm, whereas in the non-reactive zone (non-red background), the grid spacing is larger, with a maximum of 34.19 µm.

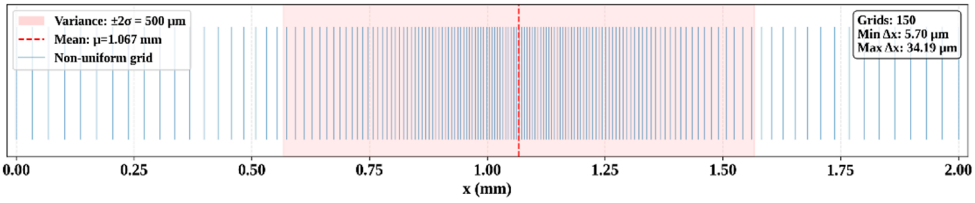
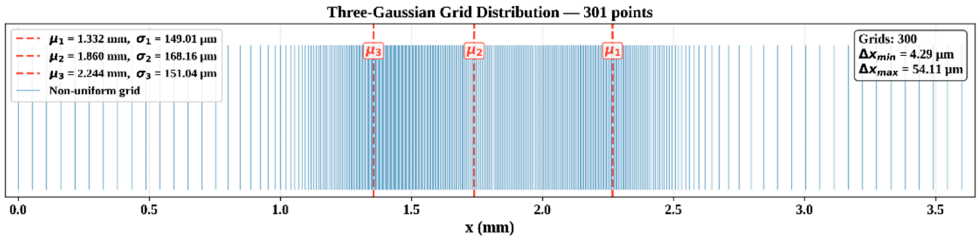


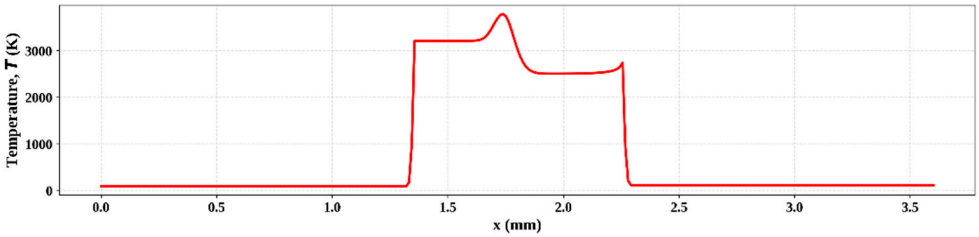
Figure 2. Schematic diagram of the single Gaussian non-uniform grid distribution.

When the flame is subjected to a high strain rate, the multi-branch flame structure is compressed into a single-peak structure, and a single Gaussian non-uniform grid can be used, which is suitable for extinction limit calculations. However, when discussing the

multi-branch flame structure and its sensitivity analysis, a low strain rate is typically employed to facilitate the observation of the variations in the oxidizer-rich premixed flamelet, the fuel-rich premixed flamelet, and the diffusion flamelet. Therefore, to accurately capture these three flamelets, a triple Gaussian non-uniform grid is adopted. Specifically, the positions of the oxidizer-rich premixed flamelet, the fuel-rich premixed flamelet, and the diffusion flamelet are set as the means of the Gaussian functions. Figure 3 presents a schematic of the triple Gaussian non-uniform grid along with the corresponding temperature distribution.



(**a**) triple Gaussian non-uniform grid distribution



(**b**) corresponding temperature distribution

Figure 3. Schematic diagram of the triple Gaussian non-uniform grid distribution along with the corresponding temperature distribution.

Here, the means μ_1, μ_2, and μ_3 represent the positions of the left oxidizer-rich premixed flamelet, the diffusion flamelet, and the right fuel-rich premixed flamelet, respectively. The standard deviations σ_1, σ_2, and σ_3 control the extent of the grid clustering region around each corresponding flamelet.

2.7.2. Extinction Limit Calculation Approach

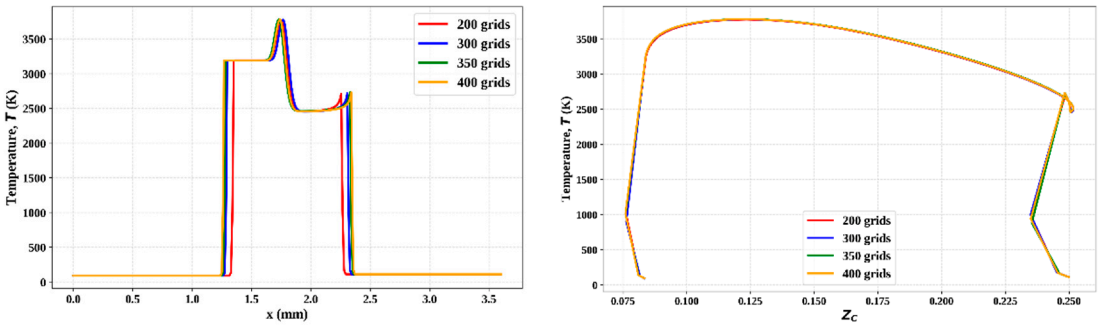
The extinction strain rate is determined through a continuation procedure based on nozzle-separation and inlet-velocity adjustments. Starting from a stable burning solution at the reference configuration, the nozzle separation distance is progressively reduced, and the inlet velocities are adjusted upward so that the global strain rate calculated from Equation (1) increases step by step. The converged solution at each condition is used as the initial solution for the subsequent higher-strain calculation. The extinction limit is identified when a stable burning solution can no longer be obtained, and the extinction strain rate is reported as the highest strain rate at which a stable flame solution is sustained. During this procedure, the Gaussian-grid parameters are adjusted to resolve the compressed reaction zone, while the inlet velocities remain below 10 ms^{-1} to ensure subsonic flow conditions 13.

3. Model and Algorithm Validation

3.1. Grid Independence Validation

Numerical simulations of the standard multi-branch flame case described in Section 2.6 were performed using the RF model with varying grid resolutions. Figure 4 presents temperature distributions of the multi-branched flames in both physical and mixture

fraction spaces for 200, 300, 350 and 400 grids. The mixture fraction is calculated as follows: $Z_C = \sum_k \frac{a_{C,k} M_C}{M_k} Y_k$, where $a_{C,k}$ denotes the number of carbon atoms in species k, M_C denotes the atomic mass of carbon, M_k denotes the molar mass of species k, and Y_k denotes the mass fraction of species k. As shown in the figure, under different grid resolutions, once the number of grids reaches 300, the errors in both flame thickness and peak temperature in physical space are negligible. Furthermore, in the mixture fraction space, the differences in temperature distribution are almost imperceptible. Moreover, the extinction limits computed at different grid resolutions are virtually identical, indicating that the grid size has no effect on the extinction limit. Therefore, to reduce computational cost and improve efficiency, a Gaussian non-uniform grid with 350 grids is adopted in the present study.



(**a**) physical space (**b**) mixture fraction space

Figure 4. Temperature distributions of multi-branched flames in physical and mixture fraction spaces with 200, 300, 350 and 400 grids in (**a**) physical and (**b**) mixture fraction spaces.

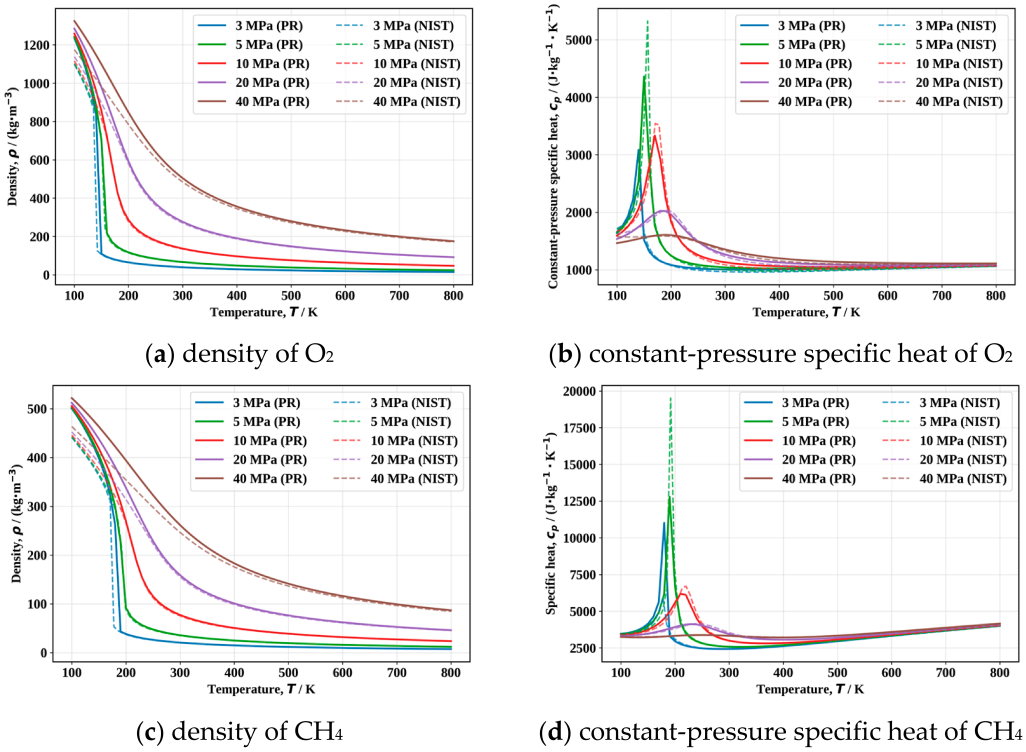
3.2. Model Validation

3.2.1. Thermophysical Properties

The critical temperatures and pressures of species in liquid-oxygen/methane combustion are summarized in Table 1. During the combustion process, oxygen (O_2) and methane (CH_4) are injected from the inlets as propellants to undergo counterflow combustion. Throughout this process, the reactants transition from subcritical to supercritical temperatures, thereby entering a transcritical state. In contrast, the reaction products remain in the supercritical state from the moment they are generated by chemical reactions, meaning that the abrupt variations near their critical points do not need to be considered. Figure 5 illustrates the density (ρ) and specific heat at constant pressure (c_p) of O_2 and CH_4, calculated using the Peng–Robinson (PR) equation of state (solid lines) and NIST [36] (dashed lines) over a pressure range of 3 MPa to 40 MPa. The results indicate that the PR equation of state agrees well with the NIST database and is capable of capturing the thermodynamic behavior of these substances across different states. While the thermophysical properties of O_2 and CH_4 do not exhibit abrupt changes under subcritical and supercritical conditions, they undergo significant variations in the transcritical regime (i.e., in the vicinity of the critical point). Therefore, a real-gas equation of state must be employed under transcritical conditions to accurately capture this phenomenon, thereby ensuring the accuracy of numerical simulations and preventing non-physical solutions.

Table 1. The critical temperatures and pressures of species in methane/oxygen combustion.

Parameter	CH_4	O_2	H_2O	CO_2	CO
P_{cr}, MPa	4.59	5.04	22.12	7.38	3.50
T_{cr}, K	190.6	154.6	647.3	304.2	132.9



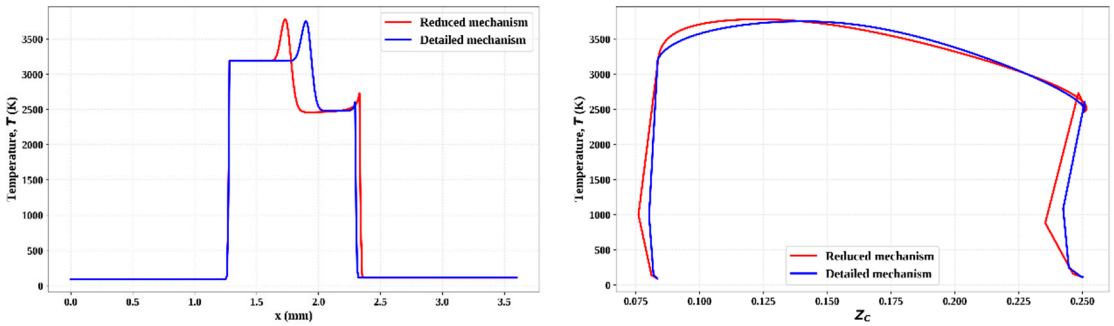
(**a**) density of O_2 (**b**) constant-pressure specific heat of O_2

(**c**) density of CH_4 (**d**) constant-pressure specific heat of CH_4

Figure 5. Effects of temperature and pressure on the thermophysical properties of O_2 and CH_4 calculated using the PR equation of state: (**a**) density of O_2, (**b**) specific heat of O_2, (**c**) density of CH_4, and (**d**) constant-pressure specific heat of CH_4.

3.2.2. Chemical Reaction Mechanism Validation

Figure 6 presents a comparison of the temperature profiles for liquid-oxygen/methane laminar counterflow multi-branched flames, calculated using the reduced mechanism and the detailed mechanism in physical and mixture fraction spaces. The flames were computed using RF model under the standard case from Section 2.6: $p = 30$ MPa, $a = 500\ \mathrm{s}^{-1}$, $\mathrm{T_f} = 110$ K, $\mathrm{T_o} = 90$ K, $\varphi_o = 0.5$, $\varphi_f = 2.0$. The temperature profiles predicted by the Laurent reduced mechanism agree closely with those obtained using GRI-Mech 3.0 in both physical and mixture-fraction spaces. In particular, the two mechanisms predict similar peak-temperature levels and overall multi-branch flame structures at the reference condition. This comparison supports the use of the Laurent reduced mechanism for the present transcritical liquid-oxygen/methane counterflow calculations. The Laurent mechanism is therefore employed in the subsequent simulations to reduce the computational cost while retaining the principal thermal characteristics of the flame.

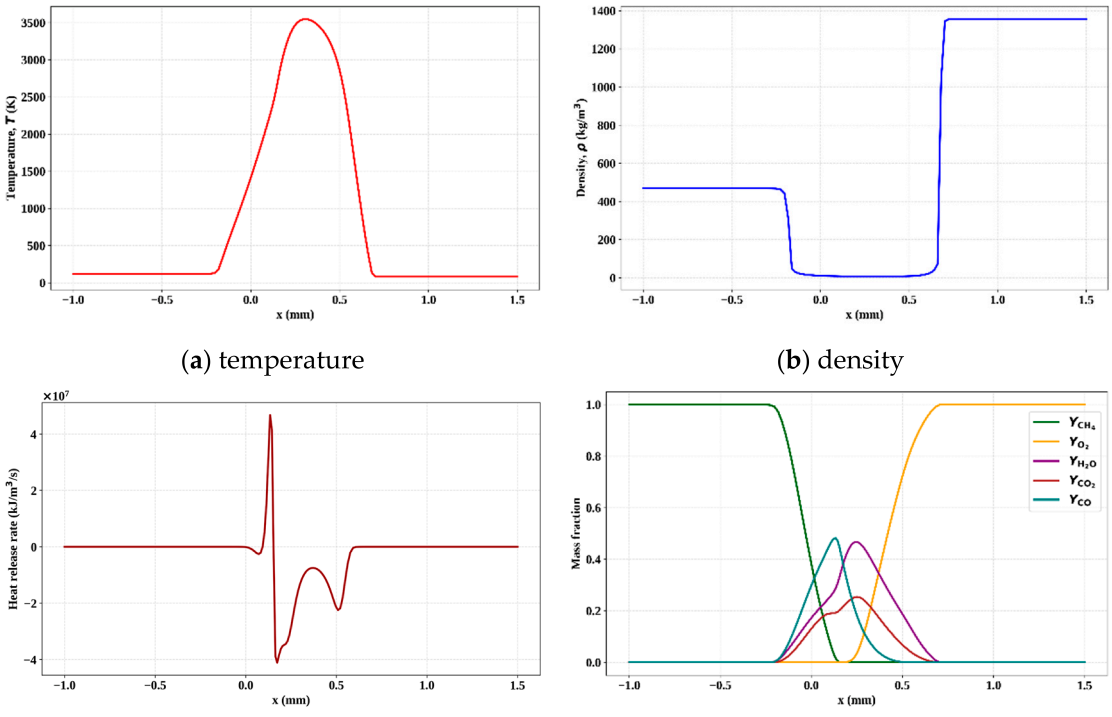


(**a**) physical space (**b**) mixture fraction space

Figure 6. Comparison of temperature of multi-branched flames based on reduced and detailed mechanisms in (**a**) physical and (**b**) mixture fraction spaces.

3.3. Algorithm Validation

Given the absence of published studies on transcritical multi-branch flames in the current literature, the present study validates the proposed model and algorithm using a transcritical laminar counterflow diffusion flame. Specifically, the CH_4/O_2 laminar counterflow diffusion flame described in Section 4.3 of Pons et al. [37] was simulated under the following conditions: a pressure of 7 MPa, an oxygen inlet temperature of 80 K, a methane inlet temperature of 120 K, a strain rate of 20 s^{-1}, and a computational domain length of 2.5 mm. The flame was numerically simulated using the reduced mechanism and PF model. Figure 7 presents the flame structure of a CH_4/O_2 laminar counterflow diffusion flame, including the distributions of temperature, density, and major species (CH_4, O_2, CO_2, H_2O, CO) mass fractions. Figure 7a shows that the temperature distribution exhibits good symmetry, with a peak flame temperature of 3546.8 K located at $x = 0.307$ mm. Figure 7b shows that the density distribution displays two regions of steep gradient, corresponding to the onset of chemical reactions. Figure 7c shows that the maximum heat release rate is approximately 4.67×10^{10} KJ/m^3/s. Figure 7d shows that the consumption of CH_4 and O_2, as well as the formation of H_2O, CO_2, and CO, are well correlated with the distributions of density, temperature, and heat release rate. The above computational results are in good agreement with the flame characteristics and distribution trends shown in Figures of Section 4.3 of Pons et al. [37], thereby validating the effectiveness of the present laminar counterflow flame calculation method. For numerical simulations of laminar counterflow multi-branch flames, it is only necessary to adjust the inlet temperature, mass flow rate, and species composition accordingly.



(**a**) temperature (**b**) density

(**c**) heat release rate (**d**) mass fraction

Figure 7. Present calculation of a transcritical CH_4/O_2 laminar counterflow diffusion flame under the operating conditions reported by Pons et al. [37] (Section 4.3): $p = 7$ MPa, $T_o = 80$ K, $T_f = 120$ K, $a = 20$ s^{-1} and $L = 2.5$ mm. (**a**) Temperature, (**b**) density, (**c**) heat release rate, (**d**) mass fraction.

Wang et al. [13] computed the extinction strain rate of stoichiometric ($\varphi = 1$) methane/oxygen laminar counterflow diffusion flames under high-pressure conditions,

obtaining values on the order of 10^6 to 10^7 s^{-1}, and concluded that the extinction strain rate increases monotonically with pressure. However, research on the extinction limits of multi-branch flames under high-pressure conditions remains absent in the literature. Existing studies have only addressed the extinction limits of diluted laminar counterflow flames at subcritical pressures. To validate the effectiveness of the extinction limit calculation method employed in the present study, two validation cases are considered. First, Lee et al. [38] numerically simulated a (CH_4 + N_2)/air laminar counterflow flame under the following conditions: $p = 4$ atm, $T_o = T_f = 300$ K, and CH_4:N_2 = 5:5. The simulation was performed using the ideal-gas equation of state and the multicomponent transport model. The extinction strain rate reported in Lee et al. [38] is 372 s^{-1}, while the present calculation yields 374.9 s^{-1}, corresponding to a relative error of only 0.77%. Second, Shih [39] numerically simulated an $H_2/O_2/CO_2$ laminar counterflow flame under the following conditions: $p = 1$ atm and $T_o = T_f = 300$ K, with an oxidizer composition of H_2:CO_2 = 1:1 and a fuel composition of O_2:CO_2 = 1:1. The simulation was performed using the ideal-gas equation of state and the multicomponent transport model. Figure 8 presents the variation in the maximum temperature with strain rate for the $H_2/O_2/CO_2$ laminar counterflow flame. The extinction limit computed in the present study is 2.232×10^4 s^{-1}. The trend of the maximum temperature as a function of strain rate is in good agreement with Figure 6 of Shih [39]. These validation results demonstrate the reliability and accuracy of the present extinction limit calculation method.

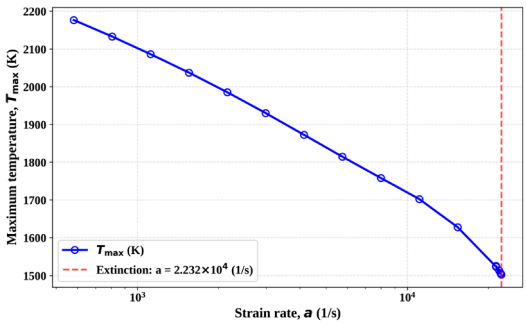


Figure 8. The variation in the maximum temperature with strain rate for the $H_2/O_2/CO_2$ laminar counterflow flame.

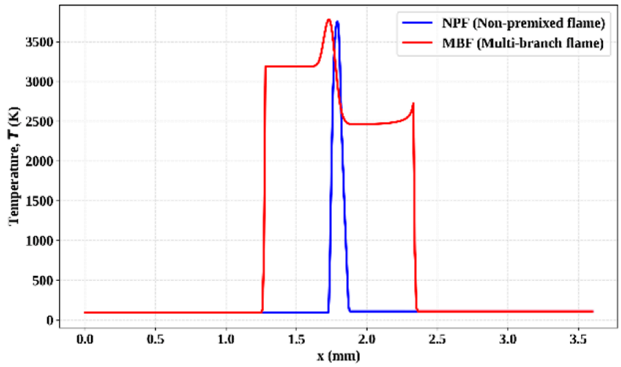
4. Results and Discussion

This section presents the numerical results for transcritical laminar counterflow multi-branch flames of liquid-oxygen/methane. The discussion proceeds from the basic flame structure to model sensitivity and then to operating-parameter effects. First, the multi-branch flame is compared with a non-premixed counterflow flame to identify the role of the premixed branches. Next, IF, PRF, and RF models are compared to determine the dominant real-fluid correction. Finally, the effects of pressure and oxidizer/fuel inlet temperature on thermodynamic structure, heat release, and extinction limits are analyzed. For figures with multiple subplots, the discussion explicitly connects each plotted quantity with the corresponding physical mechanism.

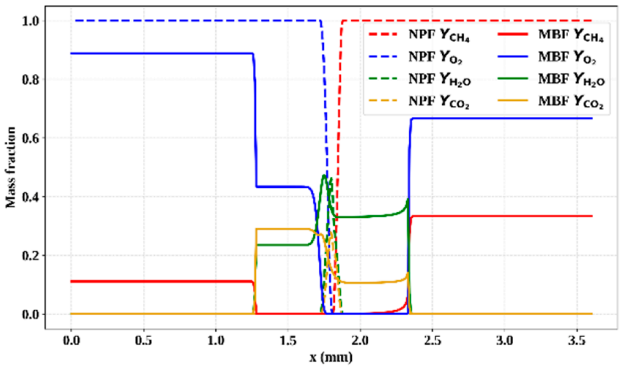
4.1. Basic Characteristics of Multi-Branch Flames

Figure 9 compares the temperature, major-species mass fractions, and axial velocity of a non-premixed flame and a multi-branch flame, both computed with the RF model. Operating conditions for both flames are as follows: $p = 30$ MPa, $a = 500$ s^{-1}, $T_f = 110$ K, and $T_o = 90$ K; and for the multi-branch flame: $\varphi_o = 0.5$ and $\varphi_f = 2.0$. Figure 9a shows that the non-premixed flame has a single temperature maximum near the central reaction zone, whereas the multi-branch flame develops two high-temperature plateaus and a higher

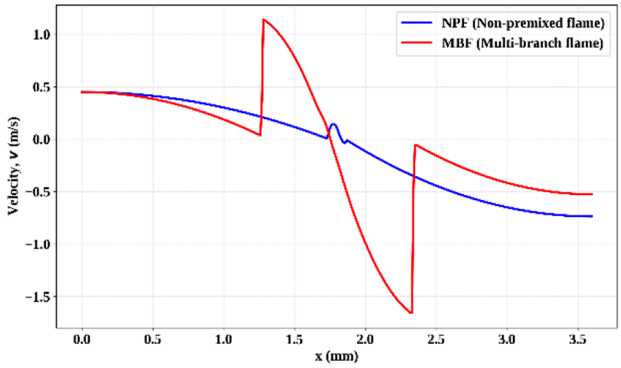
central temperature peak. The plateaus are generated by the oxidizer-rich and fuel-rich premixed branches before the central diffusion reaction becomes dominant. Figure 9b confirms this sequence through the species distributions: CH_4 and O_2 are consumed first in the premixed branches, while H_2O and CO_2 accumulate in the product regions and continue to participate in the central diffusion-reaction zone. Figure 9c shows that the non-premixed flame has a sharper axial-velocity variation near ignition ($x \approx 0.9 \sim 1.1$ mm) because heat release occurs from a colder mixing layer. In the multi-branch flame, the diffusion branch is fed by already heated products from the premixed branches, resulting in a weaker velocity gradient and a broader thermal structure. Direct comparison of the extinction limits between the diffusion flame and the multi-branch flame is not feasible, as they operate at different equivalence ratios. This quantitative contrast shows that the premixed branches can modify the flame topology.



(**a**) temperature



(**b**) mass fraction distributions



(**c**) axial velocity

Figure 9. Comparison of non-premixed and multi-branch flames under the PRF model: (**a**) Temperature, (**b**) CH_4, O_2, H_2O, and CO_2 mass fractions, and (**c**) axial velocity.

The stabilization mechanism inferred from the comparison in Figure 9 is summarized in Figure 10. In the multi-branch flame, the oxidizer-rich and fuel-rich premixed branches release heat before the central diffusion reaction becomes dominant. This early heat release forms two high-temperature plateaus and transports hot products and radicals toward the stagnation region. As a result, the central diffusion branch is sustained by a preheated, partially reacted mixture rather than being ignited from a cold mixing layer. The stabilized diffusion branch then helps maintain the coupled multi-branch structure under stronger aerodynamic strain. This closed-loop interaction increases the effective flame thickness, enhancing heat retention in the reaction zone.

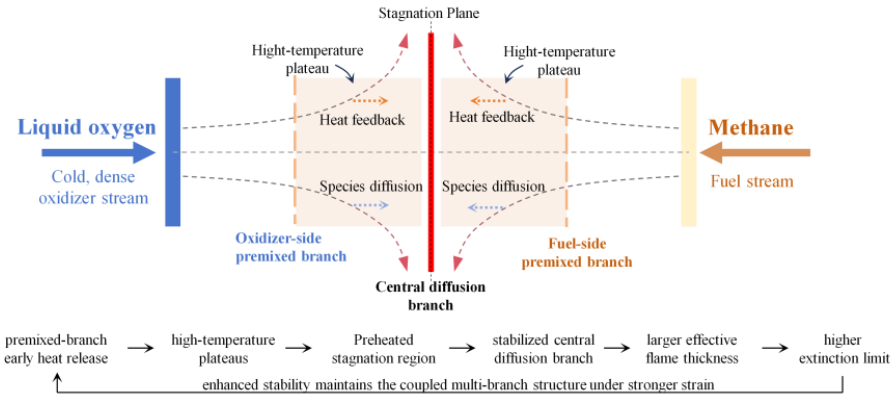
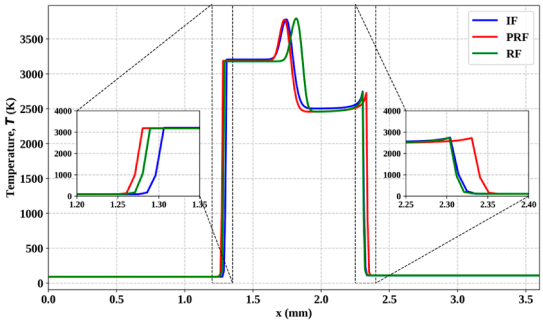


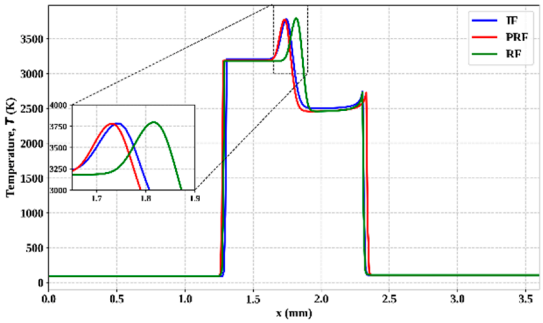
Figure 10. Closed-loop stabilization mechanism of the laminar counterflow multi-branch flame. The oxidizer-rich and fuel-rich premixed branches generate early heat release and high-temperature plateaus, which preheat the stagnation-region mixture and sustain the central diffusion branch. The stabilized diffusion branch, in turn, helps maintain the coupled multi-branch structure under stronger strain, leading to a larger effective flame thickness, stronger heat retention, and a higher extinction strain rate.

4.2. Effects of Real-Fluid Models on Simulation Results

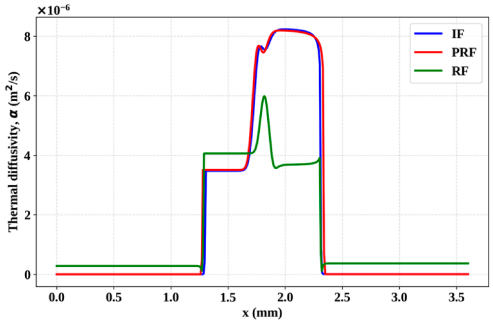
Figure 11 isolates the influence of thermophysical-property modeling on the multi-branch flame. In Figure 11a, the PRF model predicts the most upstream ignition locations. In the oxidizer-rich premixed region, the RF model predicts a slightly more upstream ignition location compared to the IF model, while in the fuel-rich premixed region, the ignition locations predicted by the RF and IF models show almost no difference. This ordering indicates that the equation-of-state correction significantly promotes earlier ignition, whereas the high-pressure transport correction in the RF model reduces upstream heat diffusion in the preheat zone, thereby delaying ignition of the premixed branches. This effect is primarily concentrated in the low- and intermediate-temperature regions of the flame, where the real-fluid transport properties remain highly sensitive to pressure and temperature. In the central flame-peak region shown in Figure 11b, the peak temperature follows the order RF > IF > PRF. This ordering results from the competition between two effects. Real-fluid thermodynamics increases the heat capacity of the colder, non-reacting mixture, which lowers the temperature rise in the high-temperature plateaus, whereas the high-pressure transport correction in the RF model reduces thermal diffusivity in the central high-temperature branch and therefore limits heat loss. Figure 11c directly shows this lower RF thermal diffusivity near the diffusion branch, and Figure 11d shows the larger real-fluid constant-pressure specific heat in the non-reacting region. Thus, the flame topology is robust, but the local temperature level and heat-retention capability are sensitive to the selected thermophysical-property model.



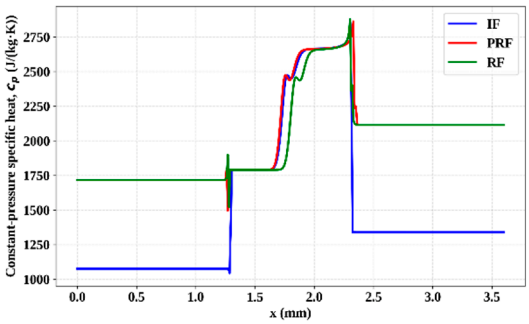
(**a**) temperature (magnified premixed reaction zone)



(**b**) temperature (magnified flame peak zone)



(**c**) thermal diffusivity



(**d**) constant-pressure specific heat

Figure 11. Multi-branch flame characteristics predicted by different thermophysical-property models: (**a**) Temperature in the premixed reaction zone, (**b**) temperature near the central flame peak, (**c**) thermal diffusivity, and (**d**) constant-pressure specific heat.

As the strain rate (a) increases, the convective effect of the counterflow field strengthens, the premixed ignition locations shift progressively toward the stagnation plane, and the overall flame thickness decreases. This thinning reflects the competition between the flow residence time and the chemical reaction time. When the strain rate exceeds the critical extinction value (a_{ext}), the flow residence time becomes too short for chemical heat release to balance convective and diffusive losses. Reactants are rapidly swept away from the reaction zone, the coupled premixed and diffusion flame branches can no longer be

sustained, and the flame extinguishes. The predicted extinction limits differ significantly among the thermophysical-property models: $a_{ext,IF} = 3.306 \times 10^6\ s^{-1}$ for the IF model, $a_{ext,PRF} = 3.256 \times 10^6\ s^{-1}$ for the PRF model, and $a_{ext,RF} = 3.256 \times 10^6\ s^{-1}$ for the RF model. Therefore, the ideal-fluid treatment slightly overpredicts the extinction limit by approximately 1.5% relative to the real-fluid treatments under the present reference condition. The identical PRF and RF results show that the high-pressure transport correction has a negligible influence on the extinction threshold. Nevertheless, the real-fluid treatments modify the ignition location, local temperature distribution, constant-pressure specific heat, and thermal diffusivity. The PRF model is therefore used for the subsequent parametric analysis because it reproduces the RF extinction response while avoiding the additional computational cost of the full transport correction.

The model-dependent differences in the results shown in Figure 11 and the extinction strain rate are summarized in Table 2. The table combines the quantitative extinction limits reported above with the qualitative trends directly supported by the temperature, thermal-diffusivity, and heat-capacity profiles.

Table 2. Comparison of key flame characteristics predicted by the IF, PRF, and RF models.

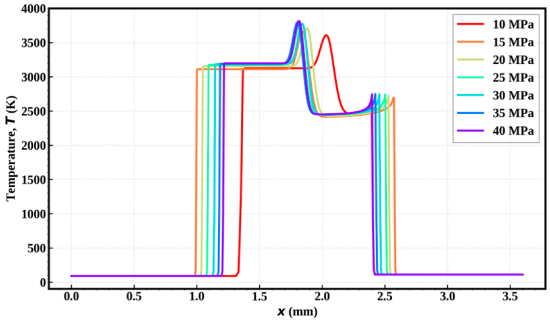
Characteristic	IF Model	PRF Model	RF Model
Thermodynamic treatment	Ideal-fluid thermodynamics	Real-fluid thermodynamics	Real-fluid thermodynamics
Transport treatment	Ideal-fluid transport	Ideal-fluid transport	High-pressure corrected transport
Overall flame topology	Three-branch structure retained	Three-branch structure retained	Three-branch structure retained
Premixed ignition location	Slightly downstream of PRF	Slightly upstream of RF	Between PRF and IF
Central peak temperature	Intermediate	Lowest	Highest
Non-reacting-region c_p	Lower than PRF/RF	Higher due to real-fluid thermodynamics	Similar to PRF
Thermal diffusivity in the central high-temperature branch	No high-pressure transport correction	No high-pressure transport correction	Lower value, reducing heat loss
Extinction strain rate	$3.306 \times 10^6\ s^{-1}$	$3.256 \times 10^6\ s^{-1}$	$3.256 \times 10^6\ s^{-1}$
Model implication	Slightly overpredicts the extinction limit relative to PRF/RF at the reference condition	Captures the RF extinction limit with lower model complexity	Most complete model; used as the reference for assessing corrections

Note: Only the extinction strain rate is reported as a numerical quantity because it is explicitly quantified in the present results; other entries summarize trends established from Figure 11.

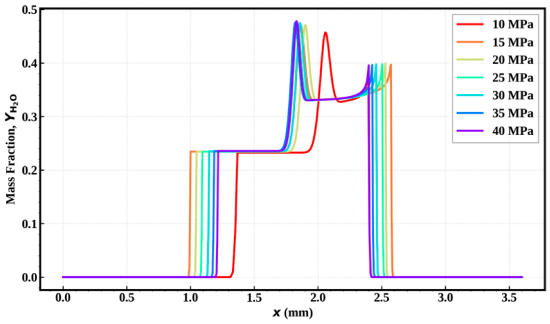
4.3. Influence of Operating Pressure on Flame Characteristics

Figure 12 presents the influence of operating pressure (from 10 MPa to 40 MPa) on the structure and thermodynamic characteristics of the multi-branch flame. All cases in this section are calculated from the standard operating condition using the PRF model. Figure 12a shows that the temperature field retains a typical multi-branch structure at all investigated pressures, including two premixed branches on the fuel-rich and oxidizer-rich sides and a central diffusion-dominated branch. As the operating pressure increases, the premixed ignition locations generally move farther from their original low-pressure positions, indicating that the local ignition process is modified by pressure-dependent real-fluid thermodynamic properties. A nonmonotonic behavior is observed when the pressure increases from 10 MPa to 15 MPa, where the ignition location shifts slightly upstream rather than following the overall downstream trend. This indicates that the pressure effect cannot be interpreted only as a monotonic increase in reactant concentration or chemical

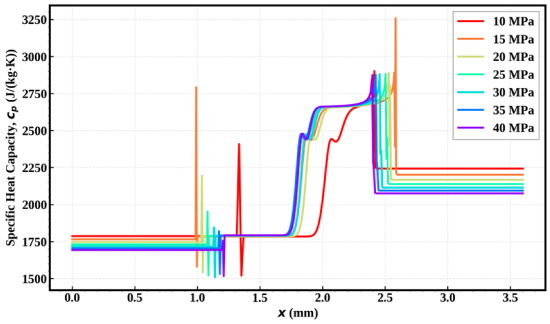
reaction rate; instead, it is strongly coupled with the local pseudo-critical behavior of the reacting mixture.



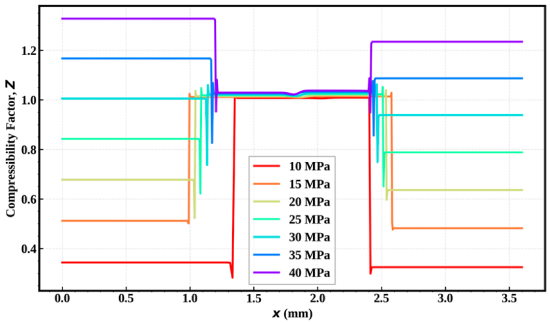
(**a**) temperature



(**b**) mass fraction of product water



(**c**) constant-pressure specific heat



(**d**) compressibility factor

Figure 12. Effect of operating pressure (from 10 MPa to 40 MPa) on multi-branch flame structure: (**a**) Temperature, (**b**) product-water mass fraction, (**c**) constant-pressure specific heat, and (**d**) compressibility factor.

The origin of this anomalous response can be understood from the product-water distribution shown in Figure 12b. Water is mainly generated in the premixed reaction zones, and its critical pressure ($p_{c,H_2O} = 22.12$ MPa) is much higher than those of methane and

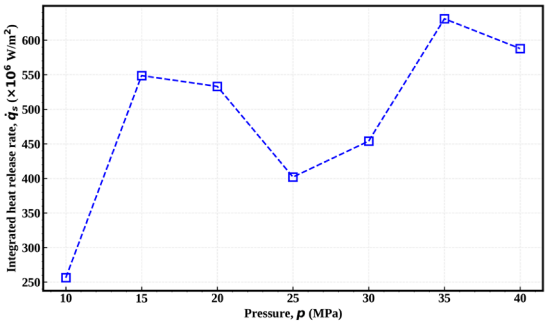
oxygen ($p_{c,ch_4} = 4.60$ MPa, $p_{c,o_2} = 5.05$ MPa). Therefore, the formation of water changes the local mixture composition and increases the pseudo-critical pressure of the reacting mixture in the premixed branches. As a result, the flame can pass through a thermodynamically sensitive region near the lower-pressure cases, especially around 10 MPa. In this region, small changes in pressure may cause large variations in real-fluid properties, which in turn modify heat capacity, heat storage, and ignition behavior. This explains why the ignition position does not vary monotonically between 10 MPa and 15 MPa.

Figure 12c further supports this interpretation by showing the distribution of the constant-pressure specific heat. A pronounced variation in heat capacity Δc_p appears in the premixed reaction region at 10 MPa, indicating that the local mixture state is close to the pseudo-critical region. In this region, a large c_p means that a larger amount of heat is required to produce the same temperature rise, so the temperature field and ignition location become highly sensitive to the thermodynamic path of the mixture. As the pressure increases beyond this sensitive region, the Δc_p becomes less abrupt, and the pressure effect on the flame structure becomes more gradual. Therefore, the pressure-induced change in the premixed branches is mainly governed by the combined effects of water formation, pseudo-critical property variation, and heat-capacity enhancement.

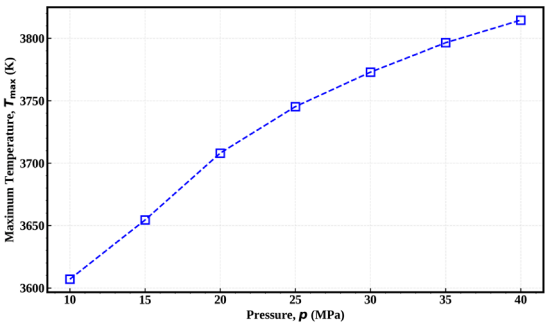
Figure 12d shows the corresponding variation in the compressibility factor Z. The compressibility factor is defined as $Z = p/(\rho R_m T)$, where p, ρ, T, and R_m denote pressure, density, temperature, and the mixture gas constant, respectively. In the non-reacting region, Z increases with operating pressure and gradually changes from a value below unity to a value above unity. This trend indicates a transition from attraction-dominated real-fluid behavior to repulsion-dominated behavior as pressure increases. The compressibility-factor variation is particularly important in the cold non-reacting region, where the fluid state is closer to the transcritical regime and real-gas effects are more pronounced. By contrast, the central non-premixed reaction zone is less sensitive to pressure-induced thermodynamic anomalies because it remains at high temperature and is already in a supercritical state. Overall, Figure 12 demonstrates that the operating pressure mainly affects the non-reacting region and the premixed reaction branches, while its direct influence on the central diffusion branch is comparatively weaker. The observed pressure dependence of the multi-branch flame is therefore controlled by the coupling among product-water formation, pseudo-critical heat-capacity variation, and real-fluid compressibility effects.

Figure 13 connects these property changes to flame intensity. Figure 13a shows that the integrated heat release rate increases with pressure, because the molar concentrations of the fuel and oxidizer are proportional to pressure, and the mass flow rate of fuel passing through the reaction zone increases under the same flame area, thereby enhancing heat release. However, in the range of 15 MPa to 25 MPa, the integrated heat release rate exhibits an anomalous decreasing behavior. This is because the compressibility factor predicted by the PR EOS in the premixed region crosses the critical transition of ($Z = 1$), and the formation of water ($p_c = 22.12$ MPa) leads to anomalies in the constant-pressure specific heat and density predicted by the PR equation of state. Figure 13b shows that the maximum flame temperature also rises with increasing pressure, because the number density of reactant molecules increases, accelerating the chemical reaction rate. Over the range of 10 MPa to 40 MPa, the maximum temperature increases by approximately 207 K. The increase is more pronounced at lower pressures and tends to saturate at higher pressures, as the dissociation suppression effect gradually approaches its limit at high densities. Figure 13c shows that as pressure increases, the thermal diffusivity in the diffusion branch decreases, thereby reducing heat loss from the high-temperature zone. This is because the density increases with pressure, while the thermal conductivity cannot keep pace with the density increase, causing a significant drop in thermal diffusivity.

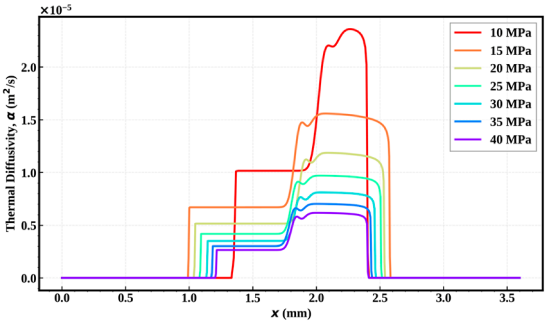
Consequently, the reduced thermal diffusivity concentrates more heat within the flame front, which is the fundamental reason why the high-pressure flamelet becomes thinner. This heat concentration, in turn, helps sustain a higher maximum temperature.



(**a**) integrated heat release rate



(**b**) maximum flame temperature



(**c**) thermal diffusivity

Figure 13. Effect of operating pressure on multi-branch flame characteristics: (**a**) integrated heat release rate, (**b**) maximum flame temperature, and (**c**) thermal diffusivity.

Figure 14 summarizes the resulting pressure dependence of the extinction limit. The extinction strain rate of the multi-branch flame increases nearly linearly from 9.336×10^5 s^{-1} at 10 MPa to 4.867×10^6 s^{-1} at 40 MPa. This trend is consistent with the combined effects shown in Figures 12 and 13: increasing pressure raises reactant concentration, strengthens heat release, and reduces diffusive heat loss. In contrast to a conventional non-premixed counterflow flame, whose extinction response is more limited once the central reaction zone is established, the multi-branch flame benefits from pressure-enhanced premixed branches that continue to preheat and stabilize the central diffusion branch. The approximately linear dependence in the present pressure range suggests that pressure enlarges the stable operating window of the idealized multi-branch flame primarily by improving the heat-release-to-transport balance.

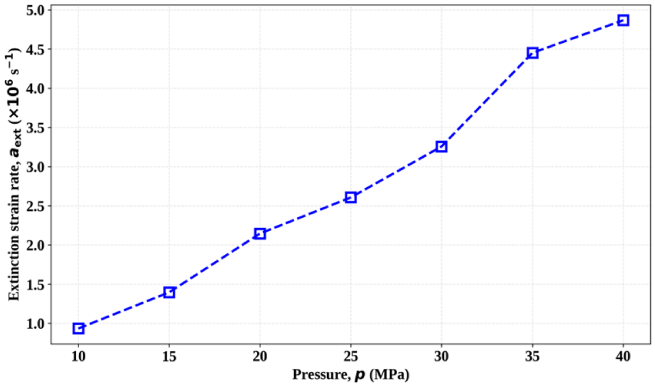
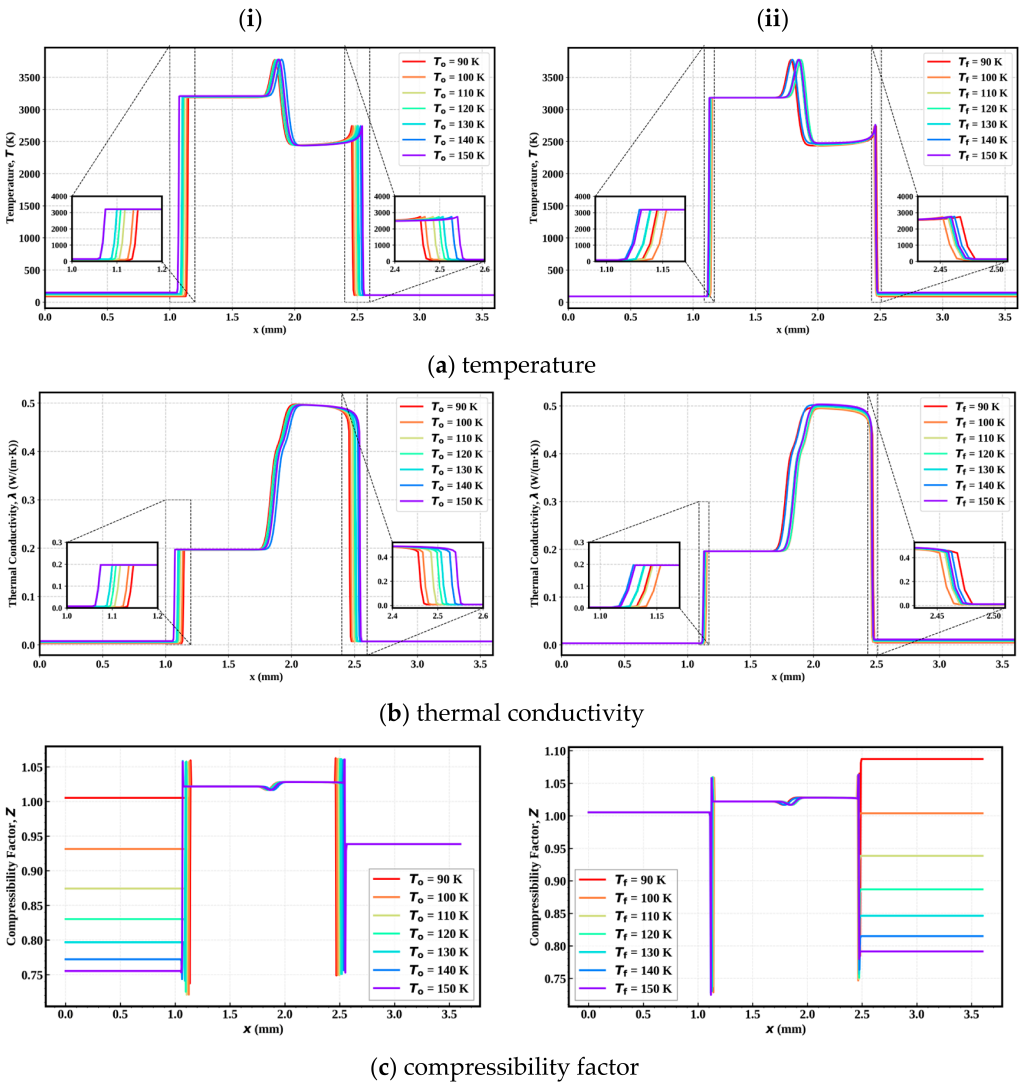


Figure 14. Extinction strain rate of multi-branch flames as a function of operating pressure from 10 MPa to 40 MPa.

4.4. Influence of Inlet Temperature on Flame Characteristics

Figure 15 compares the effects of oxidizer and fuel inlet temperatures from 90 K to 150 K (Oxidizer: $p = 30$ MPa, $a = 500$ s^{-1}, $T_f = 110$ K, $T_o = 90$–150 K, $\varphi_o = 0.5$, $\varphi_f = 2.0$; Fuel: $p = 30$ MPa, $a = 500$ s^{-1}, $T_f = 90$–150 K, $T_o = 90$ K, $\varphi_o = 0.5$, $\varphi_f = 2.0$). The oxidizer-temperature sweep is evaluated with fixed fuel-side conditions, while the fuel-temperature sweep is evaluated with fixed oxidizer-side conditions; this separation makes it possible to identify asymmetric inlet-temperature effects. Figure 15a shows that increasing the oxidizer and fuel inlet temperatures has different effects on the premixed ignition locations. Raising the oxidizer inlet temperature shifts the premixed ignition locations slightly upstream, but its influence on the central high-temperature reaction zone is limited. The weak variation in the central branch indicates that the peak reaction temperature is governed primarily by high-temperature chemical kinetics and the pressure-dependent heat retention mechanism, rather than by the inlet temperature alone. The oxidizer-rich and fuel-rich premixed ignition locations exhibit a nonmonotonic variation with increasing fuel inlet temperature. Figure 15b shows that the thermal conductivity in the non-reacting region increases with the oxidizer inlet temperature, thereby promoting pre-reaction heat transfer; it exhibits a nonmonotonic variation with increasing fuel inlet temperature. Figure 15c shows that the compressibility factor decreases with inlet temperature, indicating that inlet preheating changes the balance of real-fluid molecular interactions before ignition. These results show that inlet temperature mainly affects the upstream thermodynamic and transport state, whereas the central diffusion branch remains controlled by high-temperature chemistry and pressure-dependent heat retention.

Figure 16 quantifies the effect of inlet temperature on heat-release intensity and peak temperature. Figure 16a shows that the integrated heat release rate exhibits an oscillatory variation with the oxidizer inlet temperature, while its variation with the fuel inlet temperature is significantly smaller. This is because the influence on the integrated heat release rate is primarily achieved through density changes in the premixed region, which alter the mass flow rate, and is further modulated by the nonlinear behavior of the thermophysical properties near the critical point, resulting in a nonmonotonic response. This behavior is in stark contrast to the monotonic effect of pressure. Figure 16b shows that the variation in the maximum flame temperature remains within 20 K. Therefore, changes in the inlet temperature primarily cause a redistribution of the heat release profile and upstream transport characteristics, without significantly affecting the final thermodynamic state of the central reaction zone.



(**a**) temperature

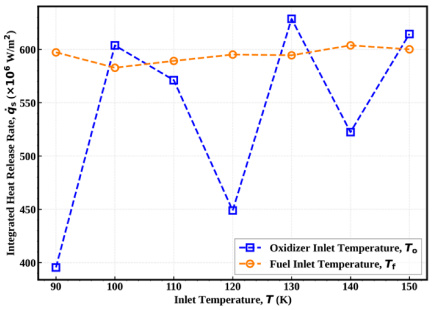
(**b**) thermal conductivity

(**c**) compressibility factor

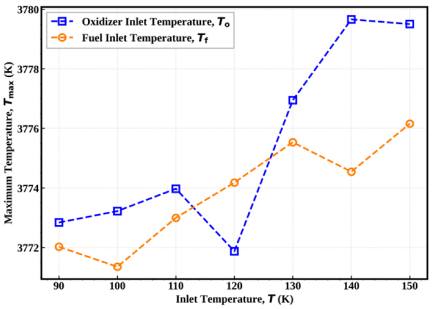
Figure 15. Effect of (**i**) oxidizer and (**ii**) fuel inlet temperatures from 90 K to 150 K on multi-branch flame characteristics: (**a**) Temperature, (**b**) thermal conductivity, and (**c**) compressibility factor.

Figure 17 presents the variation trend of the extinction limit for multi-branch flames at inlet temperatures ranging from 90 K to 150 K, showing that oxidizer and fuel preheating have different effects on flame stability. Figure 17a shows that the extinction limit exhibits a nonmonotonic dependence on the oxidizer inlet temperature, reaching a peak value of 3.892 $\times$ 10^6 s^{-1} at 130 K. In the range of 90 K to 100 K, the increase in oxidizer temperature enhances the reactivity of the oxidizer-rich premixed branch, significantly improving the flame's resistance to stretch. In the range of 100 K to 120 K, the oxygen stream crosses the pseudo-critical region, where the thermophysical properties undergo drastic variations, leading to a temporary decline in the extinction limit. In the range of 120 K to 130 K, the oxidizer-rich premixed branch becomes fully activated, the thermal diffusivity decreases, and the heat retention capacity is enhanced, causing the extinction limit to reach its peak. In the range of 130 K to 150 K, the enhancement of the oxidizer-rich premixed branch gradually approaches saturation, and further increases in oxidizer temperature yield diminishing benefits. In contrast, Figure 17b shows that the extinction limit increases slowly and monotonically with the fuel inlet temperature. This is because the thermophysical properties on the fuel side vary gradually over the range of 90 K to 150 K, and the increase in the extinction limit primarily results from the acceleration of chemical reactions driven by the higher inlet temperature. This indicates that the fuel-rich

premixed branch is insensitive to inlet temperature variations and is not the primary factor controlling extinction. Therefore, in the multi-branch flame, the oxidizer-rich premixed branch is the extinction-controlling branch, while the fuel-rich premixed branch plays a relatively minor role. These two distinctly different trends indicate that the oxidizer inlet and the fuel inlet should not be regarded as thermodynamically equivalent in high-pressure liquid-oxygen/methane combustion systems.

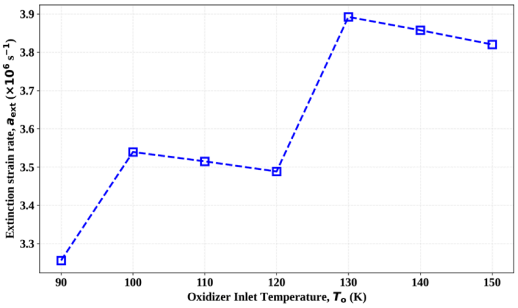


(**a**) integrated heat release rate

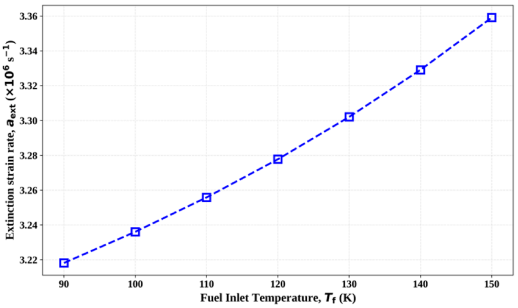


(**b**) maximum flame temperature

Figure 16. Effect of inlet temperature on (**a**) heat release rate and (**b**) maximum flame temperature of multi-branch flames.



(**a**) Extinction strain rate of T_o



(**b**) Extinction strain rate of T_f

Figure 17. Extinction strain rate of multi-branch flames as a function of oxidizer inlet temperature and fuel inlet temperature from 90 K to 150 K.

5. Conclusions

This study investigated the structure and stability of liquid-oxygen/methane laminar counterflow multi-branch flames under transcritical conditions. Flame stability was characterized by the extinction strain rate. The principal conclusions are as follows:

(1) The flame consists of oxidizer-rich and fuel-rich premixed branches coupled with a central diffusion branch. Heat release from the premixed branches creates high-temperature plateaus that preheat the stagnation-region mixture and sustain the diffusion branch.

(2) Although the IF, PRF, and RF models predict similar three-branch topologies, they produce different extinction limits. The IF model predicts 3.306×10^6 s^{-1}, whereas both PRF and RF predict 3.256×10^6 s^{-1}. Therefore, the ideal-fluid treatment slightly overpredicts the extinction limit under the present reference condition. The identical PRF and RF values indicate that high-pressure transport corrections have a negligible influence on the extinction threshold, although they still affect the local ignition location, peak temperature, and thermal diffusivity. The PRF model consequently provides an efficient representation of the RF extinction response for the present parametric study.

(3) Increasing pressure from 10 MPa to 40 MPa strengthens heat release, raises the maximum flame temperature, reduces thermal diffusion from the high-temperature region, and increases the extinction strain rate from 9.336×10^5 s^{-1} to 4.867×10^6 s^{-1}. This approximately linear increase indicates that elevated pressure improves the balance between chemical heat release and transport losses, thereby broadening the stable operating range of the multi-branch flame.

(4) Oxidizer and fuel inlet temperatures have asymmetric effects on flame stability. Oxidizer preheating produces a strong nonlinear increase in the extinction strain rate, whereas fuel preheating causes a weaker, approximately linear increase. Meanwhile, the maximum flame temperature varies by less than approximately 20 K. The stability response is therefore governed primarily by changes in real-fluid properties, transport, and branch coupling rather than by the peak flame temperature alone.

Overall, this work establishes the connection between real-fluid thermodynamics, multi-branch flame interaction, and extinction stability. The mechanisms identified not only provide insights into the coupling between real-fluid thermodynamics and multi-branch flame structures, but also offer a theoretical basis for operating condition optimization, stability margin assessment, and thermophysical model selection in full-flow staged combustion engines.

Author Contributions: Conceptualization, B.H. and W.H. (Weidong Huang); methodology, Y.B., B.H. and S.L.; software, Y.B. and W.H. (Wenfeng Hu); validation, Y.B. and B.H.; formal analysis, Y.B.; investigation, Y.B. and S.L.; resources, B.H.; data curation, Y.B., P.L. and W.H. (Wenfeng Hu); writing—original draft preparation, Y.B.; writing—review and editing, Y.B., B.H. and S.L.; visualization, Y.B. and P.L.; supervision, B.H. and W.H. (Weidong Huang); project administration, B.H.; funding acquisition, B.H. All authors have read and agreed to the published version of the manuscript.

Funding: This research was funded by the High-level Science and Technology Innovation Talent Project.

Data Availability Statement: The original contributions presented in this study are included in the article. Further inquiries can be directed to the corresponding author.

Conflicts of Interest: The authors declare no conflict of interest.

References

1. Hu, W.; Zhang, Q.-S. Research and analysis of the full-flow staged combustion cycle rocket. *J. Aerosp. Power* **2005**, *20*, 328–333.
2. Peery, S.D.; Parsley, R.C. Merits of full flow vs. conventional staged combustion cycles for reusable launch vehicle propulsion. *AIP Conf. Proc.* **1996**, *361*, 605. [CrossRef]
3. He, H.; Yu, N.; Di, S.; Cai, G.; Zhou, C.; Zheng, L. Static Equilibrium Characteristics of Full-Flow Staged Combustion Cycle Engine Under Different Propellants. *Int. J. Aerosp. Eng.* **2024**, *2024*, 7114250. [CrossRef]
4. López-Cámara, C.-F.; Juanós, A.J.; Sirignano, W.A. Strain rate and pressure effects on multi-branched counterflow flames. *Combust. Flame* **2020**, *221*, 256–269. [CrossRef]
5. Song, C.; Jin, T.; Wang, H.; Gao, Z.; Luo, K.; Fan, J. High-fidelity numerical analysis of non-premixed hydrothermal flames: Flame structure and stabilization mechanism. *Fuel* **2020**, *259*, 116162. [CrossRef]
6. Sahu, A.; Krishna, S.; Ravikrishna, R. Quantitative OH measurements and numerical investigation of H_2/CO kinetics in syngas-air counterflow diffusion flames. *Fuel* **2017**, *193*, 119–133. [CrossRef]
7. Qiao, Z.; Lv, Y.; Hickey, J.-P. Single-phase instability of intermediate flamelet states in high-pressure combustion. *Fuel* **2021**, *288*, 119736. [CrossRef]
8. Zhang, J.; Wang, J.; Chen, Y.; Li, C. Numerical study on extinction characteristics of counterflow flame in premixed NH3/CH4/air mixtures under normal temperature and pressure. *Fuel* **2023**, *334*, 126591. [CrossRef]
9. Du, H.; Hu, Y.; Zhang, J.; Wei, H.; Zhou, G.; Bai, J.; Zhang, P.; Zhou, L. Effects of ammonia addition on flame temperature profiles of n-heptane laminar diffusion flames under elevated pressures. *Fuel* **2025**, *387*, 134391. [CrossRef]
10. Darabkhani, H.G.; Zhang, Y. Methane Diffusion Flame Dynamics at Elevated Pressures. *Combust. Sci. Technol.* **2010**, *182*, 231–251. [CrossRef]
11. Ribert, G.; Zong, N.; Yang, V.; Pons, L.; Darabiha, N.; Candel, S. Counterflow diffusion flames of general fluids: Oxygen/hydrogen mixtures. *Combust. Flame* **2008**, *154*, 319–330. [CrossRef]
12. Juanós, A.J.; Sirignano, W.A. Pressure effects on real-gas laminar counterflow. *Combust. Flame* **2017**, *181*, 54–70. [CrossRef]
13. Wang, X.; Huo, H.; Yang, V. Effects of Flow Strain Rates on Counterflow Diffusion Flames at Subcritical and Supercritical Pressures: Oxygen/Methane Mixture. In Proceedings of the 52nd Aerospace Sciences Meeting, National Harbor, MD, USA, 13–17 January 2014. [CrossRef]
14. Juanós, A.J.; Sirignano, W.A. Extinction Analysis of a Methane-Oxygen Counterflow Flame at High Pressure. *Combust. Sci. Technol.* **2017**, *189*, 2180–2194. [CrossRef]
15. Stagni, A.; Brignoli, D.; Cinquanta, M.; Cuoci, A.; Frassoldati, A.; Ranzi, E.; Faravelli, T. The influence of low-temperature chemistry on partially-premixed counterflow n-heptane/air flames. *Combust. Flame* **2018**, *188*, 440–452. [CrossRef]
16. Lv, Z.; Gao, Y.; Hu, H.; Arumapperuma, G.; Fu, Q.; Han, W.; Yang, L. Numerical Investigation of Partially Premixed Flames Under Transcritical Conditions. *AIAA J.* **2024**, *62*, 1854–1863. [CrossRef]
17. Gao, Z.; Wang, H.; Song, C.; Luo, K.; Fan, J. Real-fluid effects on laminar diffusion and premixed hydrothermal flames. *J. Supercrit. Fluids* **2019**, *153*, 104566. [CrossRef]
18. Hartley, L.J.; Dold, J.W. Flame Propagation in a Nonuniform Mixture: Analysis of a Propagating Triple-Flame. *Combust. Sci. Technol.* **1991**, *80*, 23–46. [CrossRef]
19. Kioni, P.N.; Rogg, B.; Bray, K.N.C. Flame spread in laminar mixing layers: The triple flame. *Combust. Flame* **1993**, *95*, 276. [CrossRef]
20. Ruetsch, G.R.; Vervisch, L.; Liñán, A. Effects of heat release on triple flames. *Phys. Fluids* **1995**, *7*, 1447–1454. [CrossRef]
21. Owston, R.; Abraham, J. Numerical study of hydrogen triple flame response to mixture stratification, ambient temperature, pressure, and water vapor concentration. *Int. J. Hydrogen Energy* **2010**, *35*, 4723–4735. [CrossRef]
22. Bisetti, F.; Sarathy, S.; Toma, M.; Chung, S. Stabilization and structure of n-heptane tri-brachial flames in axisymmetric laminar jets. *Proc. Combust. Inst.* **2015**, *35*, 1023–1032. [CrossRef]
23. Chen, T.; Yu, S.; Liu, Y.C. Effects of pressure on propagation characteristics of methane-air edge flames within two-dimensional mixing layers: A numerical study. *Fuel* **2021**, *301*, 120857. [CrossRef]
24. Sahu, A.B.; Ravikrishna, R.V. Effect of H_2/CO Composition on Extinction Strain Rates of Counterflow Syngas Flames. *Energy Fuels* **2015**, *29*, 4586–4596. [CrossRef]
25. Kee, R.J.; E Coltrin, M.; Glarborg, P.; Zhu, H. *Chemically Reacting Flow: Theory and Practice*, 2nd ed.; John Wiley & Sons: Hoboken, NJ, USA, 2017. [CrossRef]
26. Dixon-Lewis, G. Flame structure flame reaction kinetics II. Transport phenomena in multicomponent systems. *Proc. R. Soc. London Ser. A Math. Phys. Sci.* **1968**, *307*, 111–135. [CrossRef]
27. McBride, B.J.; Zehe, M.J.; Gordon, S. *NASA Glenn Coefficients for Calculating Thermodynamic Properties of Individual Species*; NASA/TP-2002-211556; NASA: Cleveland, OH, USA, 2002. Available online: https://ntrs.nasa.gov/citations/20020085330 (accessed on 14 June 2026).

28. McBride, B.J.; Gordon, S.; Reno, M.A. *Coefficients for Calculating Thermodynamic and Transport Properties of Individual Species*; NASA TM-4513; NASA: Cleveland, OH, USA, 1993. Available online: https://ntrs.nasa.gov/citations/19940013151 (accessed on 14 June 2026).
29. Peng, D.Y.; Robinson, D.B. A New Two-Constant Equation of State. *Ind. Eng. Chem. Fundam.* **1976**, *15*, 59–64. [CrossRef]
30. Chueh, P.L.; Prausnitz, J.M. Vapor-liquid equilibria at high pressures: Calculation of partial molar volumes in nonpolar liquid mixtures. *AIChE J.* **1967**, *13*, 1099–1107. [CrossRef]
31. Chung, T.H.; Ajlan, M.; Lee, L.L.; Starling, K.E. Generalized multiparameter correlation for nonpolar and polar fluid transport properties. *Ind. Eng. Chem. Res.* **1988**, *27*, 671–679. [CrossRef]
32. Takahashi, S. Preparation of a generalized chart for the diffusion coefficients of gases at high pressures. *J. Chem. Eng. Jpn.* **1975**, *7*, 417–420. [CrossRef]
33. Laurent, C.; Esclapez, L.; Maestro, D.; Staffelbach, G.; Cuenot, B.; Selle, L.; Schmitt, T.; Duchaine, F.; Poinsot, T. Flame-wall interaction effects on the flame root stabilization mechanisms of a doubly-transcritical LO_2/LCH_4 cryogenic flame. *Proc. Combust. Inst.* **2019**, *37*, 5147–5154. [CrossRef]
34. Smith, G.P.; Golden, D.M.; Frenklach, M.; Moriarty, N.W.; Eiteneer, B.; Goldenberg, M.; Bowman, C.T.; Hanson, R.K.; Song, S.; Gardiner, W.C., Jr.; et al. GRI-Mech 3.0. Gas Research Institute. 1999. Available online: http://combustion.berkeley.edu/gri-mech/version30/text30.html (accessed on 14 June 2026).
35. David, G.G.; Harry, K.M.; Ingmar, S.; Raymond, L.S.; Bryan, W.W. *Cantera: An Object-Oriented Software Toolkit for Chemical Kinetics, Thermodynamics, and Transport Processes*, Version 3.2.0; Cantera: San Antonio, TX, USA, 2025. Available online: https://www.cantera.org (accessed on 14 June 2026).
36. Lemmon, E.W.; Ian, H.B.; Huber, M.L.; McLinden, M.O. *NIST Standard Reference Database 23: Reference Fluid Thermodynamic and Transport Properties-REFPROP*, Version 10.0; National Institute of Standards and Technology, Standard Reference Data Program: Gaithersburg, MD, USA, 2018. [CrossRef]
37. Pons, L.; Darabiha, N.; Candel, S.; Ribert, G.; Yang, V. Mass transfer and combustion in transcritical non-premixed counterflows. *Combust. Theory Model.* **2009**, *13*, 57–81. [CrossRef]
38. Lee, U.D.; Shin, H.D.; Oh, K.C.; Lee, K.H.; Lee, E.J. Extinction limit extension of unsteady counterflow diffusion flames affected by velocity change. *Combust. Flame* **2006**, *144*, 792–808. [CrossRef]
39. Shih, H.-Y. Computed extinction limits and flame structures of H_2/O_2 counterflow diffusion flames with CO_2 dilution. *Int. J. Hydrogen Energy* **2009**, *34*, 4005–4013. [CrossRef]

Disclaimer/Publisher's Note: The statements, opinions and data contained in all publications are solely those of the individual author(s) and contributor(s) and not of MDPI and/or the editor(s). MDPI and/or the editor(s) disclaim responsibility for any injury to people or property resulting from any ideas, methods, instructions or products referred to in the content.